Title

Computing inelastic neutron scattering spectra from molecular dynamics trajectories

Journal

Scientific Reports, 11(1)

ISSN

2045-2322

Authors

Harrelson, Thomas F

Dettmann, Makena

Scherer, Christoph

et al.

Publication Date

2021

DOI

10.1038/s41598-021-86771-5

Peer reviewed

Computing Inelastic Neutron Scattering Spectra from Molecular Dynamics Trajectories

Thomas F. Harrelson[1,2], Makena Dettmann[3], Christoph Scherer[4], Denis Andrienko[4], Adam J. Moulé[1], and Roland Faller[1]

[1]Department of Chemical Engineering, University of California - Davis, 1 Shields Ave, Davis, CA 95616

[2]Current Address - Molecular Foundry, Lawrence Berkeley National Laboratory, 1 Cyclotron Road, Berkeley, CA 94720

[3]Department of Materials Science and Engineering, University of California - Davis, 1 Shields Ave, Davis, CA 95616

[4]Max Planck Institute for Polymer Research, Ackermannweg 10, 55128 Mainz, Germany

Abstract

Inelastic neutron scattering experiments have the potential to provide morphological information of complex, partially crystalline, non-equilibrium morphologies. Their interpretation, however, relies on well defined models used to identify distinct contributions to the spectra. Here we propose a method that allows to directly compare INS to molecular dynamics simulations of semicrystalline/amorphous materials. We illustrate the technique by analyzing spectra of a well-studied conjugated polymer, poly(3-hexylthiophene-2,5-diyl) (P3HT) and conclude that large-scale morphologies, well beyond those accessible to ab initio techniques, are required to better represent the data.

1 Introduction

Efficient and accurate computer simulations of complex systems are the key to accelerating scientific discovery in many fields of physics, chemistry, and biology [1]. Molecular simulation has been used to provide structural and dynamical information on complex systems such as biological proteins [2, 3], polymers [4, 5, 6], lipid membranes [7], and metal-organic frameworks [8, 9, 10]. The number of molecules necessary to extract the observable quantity of interest determines the type and accuracy of the simulation. Relatively small systems consisting of a few molecules of the order of 100-1000s of atoms are simulated using density functional theory (DFT). While less accurate than wavefunction-based methods, DFT is still accurate enough to predict experimentally observable phenomena. Larger systems ($10^4 - 10^6$ atoms) must be simulated with classical, all-atom molecular dynamics (MD), or coarse-grained MD ($10^6 - 10^8$ effective atoms), which are less accurate than DFT methods, but the significantly improved computational scaling allows better sampling of phase space compensating for the accuracy reduction. The ability to predict macroscopic quantities using classical forcefields depends on the quality of its empirical parameters, which must be validated against a variety of experiments. In particular, the non-bonded parameters are parametrized from experimental densities, phase transition temperatures, solvation free energies, and heats of vaporization [11]. While fitting parameters to a small number of macroscopic observables is useful, it would be more accurate to validate against larger data sets, such as dynamical spectra, to parametrize forcefields.

Obtaining information on the dynamics of atoms within materials/fluids requires various forms of dynamical spectroscopy such as NMR, neutron scattering methods, and infrared absorption/scattering methods [12, 13]. In particular, inelastic neutron scattering (INS) experiments provide valuable information on the structure and dynamics of molecular systems such as polymers [4, 6], metal-organic frameworks [10], molecular crystals [14, 15], and crystalline oxide materials [16]. Unlike optical methods such as FTIR and Raman, INS has no selection rules based on molecular symmetry; all overtones are observable [17] increasing the density of information in the spectra. Molecular simulations must be used to interpret the spectra to fully understand all

the information present. For crystalline materials, there is a robust method for simulating INS spectra from DFT simulations [18, 19] by converting simulated phonons into spectral features. In this paper, we develop a technique for simulating INS spectra for semicrystalline/amorphous materials, which represent the majority of organic materials. For these material systems, the significant concentration of ^{1}H atoms means that coherent scattering signals are not observed. For that reason, we only consider the contribution of incoherent scattering signals.

Interpreting INS spectra for amorphous/semicrystalline materials requires simulation techniques that can handle length scales large enough to describe the structural disorder in the material. Time scales probed by inelastic neutron scattering depend on the experimental setup. Crystal analyzer neutron spectrometers (such as VISION and TOSCA) provide dynamical information over an energy range of $\sim 10 - 5000$ cm^{-1} [20], which corresponds to time scales of $\sim 1 - 1000$ fs. This makes classical, all-atom MD the ideal simulation technique for interpreting INS spectra because typical time steps in MD are of the order of 1 fs.

Developing a method for computing the inelastic neutron scattering function from time-ordered trajectories is challenging because the underlying scattering physics depend on quantum mechanical information of the dynamics of the system. This is seen in the low-temperature form of the scattering function, which is,

$$S(\vec{q},\omega) = \sum_{n,i,j} \sigma_i \frac{(\vec{q}\cdot\vec{u}_{ij})^{2n}}{n!} \exp\left[-\sum_j (\vec{q}\cdot\vec{u}_{ij})^2\right] \delta(\omega - n\omega_j) \quad (1)$$

where $\vec{q}$ is the momentum transfer vector, ω is the frequency of oscillation, σ_i is the neutron cross section for atom i, $\vec{u}_{ij}$ is the quantum-mechanical ground state displacement of mode j projected onto atom i, and n is the quantum number of the nth excitation. The exponential term in the scattering function is called the Debye-Waller factor. Eq 1 represents the probability that the neutron interacts with atom i, transferring $\hbar\vec{q}$ momentum ($\vec{q}$ is the difference between $\vec{k}_i$ and $\vec{k}_f$ in Figure 1), which excites the vibrational state of the jth oscillator to the nth overtone. Figure 1a demonstrates the physics of an inelastic neutron scattering event represented by the scattering function in eq 1: a neutron scatters off of an anharmonic oscillator (which models the atomic dynamics), transferring energy to the atom by exciting one (or several) of its vibrational modes, and exiting the sample toward the detector with a smaller wavevector. The orientation of the molecule relative to the direction of the incoming neutron is important as most atoms in a molecular solid do not vibrate isotropically. Rotation of an anisotropic oscillator changes the probabilities of excitation for all of the modes. In specific orientations, some modes are completely invisible to neutron scattering because the direction of oscillation is perpendicular to the momentum transfer of the scattering event (an example is shown in Figure 1b). This phenomenon is mathematically represented by the dot products between $\vec{q}$ and $\vec{u}_{ij}$ in eq 1. Therefore, we see that computing a scattering function requires computation of the ground state displacement of mode j projected onto atom i ($\vec{u}_{ij}$) and it's corresponding frequency (ω_j).

The most common method for computing these parameters uses DFT simulations combined with normal mode analysis [18]. The $\vec{q}$ dependence of the scattering function is assumed to follow that of inverted geometry neutron spectrometers, such as VISION [20], for which $q^2 \propto \omega$ [17]. The exact equations for q as a function of ω are determined by the instrument setup (e.g. position and type of analyzer crystals). It is also possible to use a classical forcefield in place of a density functional to calculate the dynamical matrix required to obtain the phonon eigenvectors and frequencies, which allows the simulation of phonons for systems larger than DFT can typically handle (~ 1000 atoms).

While normal mode analysis is quite useful for comparing DFT simulations to INS spectra, it becomes unfeasible for large systems typically encountered in MD simulations because of the computational requirements for diagonalizing matrices the size of three times the number of atoms in the simulation. To decrease the computational cost, previous studies comparing MD simulations to INS spectra have computed the Fourier transform of the velocity autocorrelation function (called the power spectrum). Recently, there has been some research that uses autocorrelation functions of MD simulations to obtain phonon dispersion curves [21, 22]. These methods share a lot theoretical similarities to our approach, but are limited to calculating dispersion curves for crystalline systems, which are observed from angle-resolved coherent neutron spectra (e.g. from the SEQUOIA spectrometer [23]). In addition to being more computationally expensive to simulate, most materials contain hydrogen, which means INS experiments yield an incoherent signal that does not have a well-defined dispersion curve. To simulate the incoherent INS spectra for heterogeneous materials involves calculating the the phonon density of states (pDOS) from

the velocity autocorrelation function. The pDOS is then projected onto specific atom types that strongly scatter neutrons (typically ^{1}H) and compared directly to INS spectra [4]. This method leads to inaccuracies, as the pDOS is only part of the input into the calculation of an INS spectrum from the scattering function (eq 1). The pDOS does not contain the Debye-Waller factor, the $\vec{q}$ dependence, and overtones, which means that the projected pDOS can only be used in a qualitative comparison to INS data. The inaccuracy of the pDOS method is demonstrated in Figure 1c, which shows the energy profile of a classical trajectory of a harmonic oscillator thermostatted to temperature T. Each classical mode (represented by an oscillator) would contribute to a peak at the correct frequency, but the height of the peak is proportional to T, which is not consistent with eq 1. The formulation for computing INS spectra from MD trajectories with the least number of approximations is in ref [17] (e.g. overtones, Debye-Waller factor, and $\vec{q}$ dependence), but this method still leads to inaccuracies due to the lack of frequency dependence of the anisotropic vibrational disorder, and quantum ground state atomic displacements. In this manuscript, we present a method for computing INS spectra from all-atom MD trajectories that is as correct as the normal mode-based methods used in conjunction with DFT simulations.

2 Theory

Energy resolved dynamics from MD simulations is characterized by the power spectrum, which is the Fourier transform of the velocity autocorrelation function,

$$v_i^2(\omega) = F\left\{\langle \vec{v}_i(t) \cdot \vec{v}_i(t+\tau)\rangle\right\} \tag{2}$$

in which v_i is the velocity of atom i, $F\{...\}$ represents a Fourier transform, and $\langle ...\rangle$ represents the time average. The power spectrum can be related to the eigenvectors (normal modes) and eigenvalues. To show this, we first expand the atomic velocities into contributions from the normal modes,

$$\vec{v}_i(t) = \sum_j c_{ij}\vec{\nu}_j(t) \tag{3}$$

where ν_j is the velocity of mode j along the vibrational mode coordinate, and c_{ij} is the unitary transformation matrix between the atomic basis and the vibrational basis. Even though it is possible to construct the power spectrum from the phonon eigenvectors, it is not generally possible to reconstruct the eigenvectors from the power spectrum because of potential degeneracies in the eigenspectrum.

We are assuming a harmonic approximation, which means that the velocity of the classical oscillators, $\vec{\nu}_j$, takes the form,

$$\vec{\nu}_j(t) = \vec{V}_j \cos(\omega_j t + \delta_j) \tag{4}$$

where $\vec{V}_j$ is the maximum velocity of mode j, ω_j is the frequency, and δ_j is the phase. This equation implies that the power spectrum of $\vec{v}_i$ using the expansion in eq 3 reveals independent oscillators at different frequencies,

$$v_i^2(\omega) = \sum_j \frac{|c_{ij}|^2 V_j^2}{4}\delta(\omega - \omega_j) \tag{5}$$

in which $|c_{ij}|^2$ is the probability that atom i participates in mode j. The power spectrum cannot differentiate between different modes at the same frequency. This represents a potential problem in the evaluation of strength of the vibrational eigenvectors from the power spectrum, as the change in phase between any pair of oscillators (δ_j in eq 4) impacts the observed peak height in the power spectrum. However, in eq 5 we are asserting that the oscillators are uncorrelated, which is true if the simulation has at least a weak thermostat (or weak anharmonicities) that decorrelate the oscillators. Then the relative phase differences between the oscillators average to zero, and the observed peak heights of the power spectrum are equal to the sum of each of the contributing vibrational eigenvectors.

The accuracy of simulated phonons is assessed through comparison to experimental INS spectra. Low temperature INS spectra are well described by the scattering function in eq 1 [17]. The quantum mechanical displacements ($\vec{u}_{ij}$) are not directly accessible from the atomic power spectra in MD trajectories, so we seek a connection. The magnitude of the ground state displacement of a quantum harmonic oscillator is given by,

$$u_{ij}^2(\omega_j) = \frac{|c_{ij}|^2\hbar}{2\mu_j\omega_j} \tag{6}$$

where μ_j is the reduced mass of mode j [24]. Note that every term in eq 6 is accessible from the atomic power spectra, except μ_j. To find μ_j from information in the power spectra, we use the equipartition theorem:

$$k_B T = \mu_j\langle\nu_j^2\rangle = \mu_j\frac{V_j^2}{2} \tag{7}$$

Simple rearrangement of eqs. (5) to (7) provides a

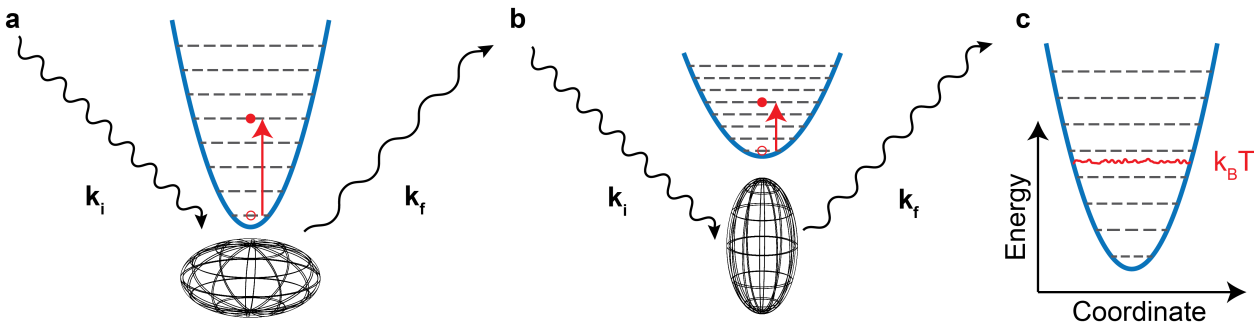

Figure 1: (a,b) Schematic depicting neutron scattering off a prolate anisotropic oscillator (oval wireframe object) in two different orientations demonstrating how molecular orientation changes the available scattering processes. In (a) the momentum transfer is directed solely along the short axis of the oscillator, creating vibrationally excitations along that axis. In (b) the oscillator is rotated such that the momentum transfer is directed along the long axis of the oscillator, which has smaller spacing between energy levels. (c) Potential energy surface for a harmonic oscillator. The quantum mechanical levels are represented by grey dashed lines, and the rough red line represents a trajectory of a classical simulation.

relationship for u_{ij}^2 as a function of the power spectrum:

$$u_i^2(\omega) = \frac{\hbar v_i^2(\omega)}{\omega k_B T} \tag{8}$$

where we have implicitly summed over all degenerate modes at a given frequency, ω, to remove the dependence on the j index. Essentially, the knowledge of the effective maximum velocity of modes at frequency ω provides the curvature of the potential energy surface shown in Figure 1c, which is directly related to the ground state displacement of a quantum mechanical object acting on the same potential energy surface (assuming the harmonic approximation holds).

The units of eq 8 are not the same as eq 6 as $v_i^2(\omega)$ has units of m^2/s instead of m^2/s^2 because of the action of the Fourier transform. The correct units are recovered with an integral over ω. Thus, eq 8 contains both $u_{i,j}$ and the delta function from the scattering law (eq 1) because the delta function, $\delta(\omega - \omega_j)$ has units of ω^{-1}. This formulation of $u_i^2(\omega)$ can be used in the scattering law under the assumption that all the oscillators have an isotropic displacement from their equilibrium positions, which is generally untrue. Thus, the scattering rate into a particular solid angle depends on the momentum scattering vector, $\vec{q}$, in eq 1.

For inverted geometry spectrometers, such as VISION at ORNL or TOSCA at ISIS, the magnitude of the momentum scattering vector changes with energy transfer, meaning the instruments are not well-equipped for independently probing the $\vec{q}$ dependence of the scattering law. In addition, it is experimentally difficult to obtain single crystals that are large enough to obtain good neutron scattering data (~ 1 g is needed [17]). Thus, crystalline powder samples are commonly used for neutron measurements, which require an orientational average over the scattering function. The orientational dependence of the scattering function is graphically depicted in Figure 1a,b, and the equation for the orientational average has no analytical solution, and must be numerically approximated. The most common approach to simplify the powder average is the "almost isotropic" approximation [17, 18]. This approach is used to approximate the powder average of the first overtone of the scattering equation ($n = 1$ in eq 1) which we write as,

$$S_{0\to1}(q,\omega_j) = \frac{1}{4\pi}\int S_{0\to1}(\vec{q},\omega_j)d\Omega \tag{9}$$

$$S_{0\to1}(\vec{q},\omega_j) = \sum_i \sigma_i(\vec{q}\cdot\vec{u}_{ij})^2 \exp\left[-\sum_j(\vec{q}\cdot\vec{u}_{ij})^2\right] \tag{10}$$

where $S_{0\to1}(q,\omega_j)$ is the powder averaged scattering function for the first overtone, and $d\Omega$ is the differential angle. The equation is restricted to a single mode j for simplicity; the full scattering function is the sum over all mode contributions. The almost isotropic ap-

proximation [17] changes this equation to:

$$S_{0\to1}(q,\omega_j) \approx \sum_i \frac{q^2}{3}\,\mathrm{Tr}(\overline{\overline{B}}_{ij})\exp\left(-q^2\alpha_{ij}\right) \quad (11)$$

$$\alpha_{ij} = \frac{1}{5}\left[\mathrm{Tr}(\overline{\overline{A}}_i) + 2\left(\frac{\overline{\overline{B}}_{ij} : \overline{\overline{A}}}{\mathrm{Tr}(\overline{\overline{B}}_j)}\right)\right] \quad (12)$$

$$\overline{\overline{B}}_{ij} = \vec{u}_{ij}\vec{u}_{ij}^T \quad (13)$$

$$\overline{\overline{A}}_i = \sum_j \overline{\overline{B}}_{ij} \quad (14)$$

where $\overline{\overline{B}}_{ij}$ is defined as the displacement tensor of atom i for mode j, and $\overline{\overline{A}}_i$ is the total displacement tensor for atom i. Eq 11 is typically used for the first overtone, while higher overtones are usually computed within the isotropic approximation [17] as the almost isotropic approximation only marginally improves accuracy while severely complicating the computation. The isotropic approximation of the Debye-Waller factor is

$$\mathrm{DWF} = \exp\left[-q^2 A_i/3\right]. \quad (15)$$

To make our formulation consistent with the almost isotropic approximation, we must create analogous versions of $\overline{\overline{A}}_i$ and $\overline{\overline{B}}_{ij}$ from MD trajectories. The power spectrum in eq 8 is analogous to the trace of $\overline{\overline{B}}_{ij}$, so we must expand the power spectrum to include all possible cross correlations between the different Cartesian components of the velocity. Thus, we define an outer-product velocity correlation function, $\langle \vec{v}_i^*(t)\vec{v}_i^T(t+\tau)\rangle$, which is a Hermitian tensor, and its corresponding Fourier transform is shown in matrix form in eq 16.

$$\vec{v}\vec{v}^T(\omega) = \begin{pmatrix} \langle|v_x(\omega)|^2\rangle & \langle v_x^*(\omega)v_y(\omega)\rangle & \langle v_x^*(\omega)v_z(\omega)\rangle \\ \langle v_y^*(\omega)v_x(\omega)\rangle & \langle|v_y(\omega)|^2\rangle & \langle v_y^*(\omega)v_z(\omega)\rangle \\ \langle v_z^*(\omega)v_x(\omega)\rangle & \langle v_z^*(\omega)v_y(\omega)\rangle & \langle|v_z(\omega)|^2\rangle \end{pmatrix} \quad (16)$$

We can replace $v_i^2(\omega)$ with $\vec{v}\vec{v}^T(\omega)$ in eq 8 to construct an analogous version of $\overline{\overline{B}}_{ij}$, which extends our formulation beyond the isotropic approximation. In this formulation, $\overline{\overline{A}}_i$ is the integral of $\overline{\overline{B}}_j$ with respect to ω. From here, our analogous versions of $\overline{\overline{A}}_i$ and $\overline{\overline{B}}_{ij}$ can be inserted into the almost isotropic approximation equation providing the scattering function of the first overtone completely in terms of the information present in a classical MD simulation.

To summarize, we have computed ground state displacements of a set of quantum harmonic oscillators from the information in the classical power spectrum, and we have approximated the powder average while accounting for anisotropies of vibrational motion. The only remaining problem is the inclusion of overtones in the simulated spectrum because the power spectrum does not contain any overtones assuming the harmonic approximation is valid. It is possible that overtones appear in highly anharmonic modes, which is why we run the molecular dynamics simulation at low temperature (which also simulates the INS experiment at low temperature). Obtaining the spectral contribution of overtones is not trivial because combination excitations need to be calculated (simultaneous excitation of two different $0 \to 1$ transitions) in addition to the principal overtones ($0 \to 2$ transitions). To obtain the full second overtone spectrum, including combination excitations, the fundamental spectrum (obtained from $\langle \vec{v}\vec{v}^T(\omega)\rangle$) is convolved with itself:

$$\overline{\overline{B}}_{0\to2}(\omega) = \overline{\overline{B}} * \overline{\overline{B}} = \int \overline{\overline{B}}(\omega')\overline{\overline{B}}(\omega-\omega')d\omega' \quad (17)$$

In principle, since $\overline{\overline{B}}$ is a matrix, the convolution produces a fourth order tensor that must be contracted into a second order tensor (to be used in the almost isotropic approximation), which we approximate as a simple matrix multiplication between $\overline{\overline{B}}$ with itself at a different frequency. To get the third overtone spectrum, we convolute $\overline{\overline{B}}_{0\to2}(\omega)$ with $\overline{\overline{B}}(\omega)$. Therefore, the spectrum of the nth overtone in INS can be computed of as the nth convolution of $\overline{\overline{B}}$ with itself. If we define the convolution as an operator, we can show that the series of convolution operators reproduces the intermediate scattering function (see Supplemental Information section 1), which has been used for analyzing all other forms of inelastic neutron scattering experiments (e.g. QENS, neutron spin echo, etc.). The intermediate scattering function is a useful starting point for which to analyze other dynamical measurements such as X-ray techniques and dynamic light scattering, meaning that our approach can be used for something other than neutron scattering measurements.

The computational workflow is as follows:

1. The atomic displacement tensor, $\overline{\overline{B}}_1$, for atom i was computed from the molecular dynamics trajectory for that atom using eqs 8 and 16.

2. Vector containing the q^2 dependence as a function of ω was computed (specific to the back scattering analyzers of the VISION spectrometer [20]),

3. The Debye-Waller factor was computed for both the isotropic and "almost isotropic" approximations.

4. The q^2 vector, the trace of the current $\overline{\overline{B}}_n(\omega)$ object (trace of this object is a vector), and the Debye-Waller factor were element-wise multiplied, and the resulting vector was multiplied by the prefactor scalar that depends on the overtone number (same as the loop counter).

5. Resulting vector was added to a total scattering function vector (initialized to zeroes).

6. The current $\overline{\overline{B}}_n$ object was convolved with the original atomic displacement tensor, $\overline{\overline{B}}_1$, which generates a new object, $\overline{\overline{B}}_{n+1}$, that corresponds to the next overtone spectrum to be computed in the next iteration of the loop.

7. The above algorithm was repeated for each overtone (total number of overtones is set at the beginning of the workflow).

We assume that the convolution operation between two matrices of functions can be approximated as another matrix that follows from standard matrix multiplication rules (e.g. $\overline{\overline{B}} * \overline{\overline{B}} = \sum_j B_{ij} * B_{jk}$), ensuring that the resulting matrix is Hermitian. Thus, each convolution operation contracts the inner indices of the resulting rank-4 tensor. The Debye-Waller factor from the "almost isotropic" approximation is used for the first overtone $n = 1$, and the isotropic approximation is used for all others. The loop index specific prefactor is assumed to be $\frac{3^{n-2}}{n!5^{n-1}}$ because it is a general relation that closely resembles the known prefactors for the first four overtones for powder averages using either isotropic or "almost isotropic" approximations [18].

If we want to extend our approach beyond the harmonic approximation, we must identify anharmonicities in the classical power spectra. The anharmonicities manifest as either (1) overtones in the harmonic power spectrum, or (2) decay rates of periodic motions, which broaden peaks in the power spectrum (typically with a Lorentzian lineshape) . The former arises from anharmonicities along the vibrational mode coordinate (see SI Figure S1b), which can be mathematically represented by coupling between energy levels on the same oscillator. The decay rates of classical motions come from coupling between energy levels on different harmonic modes (see SI Figure S1c). In principle, it is possible to approximate the different anharmonic contributions by fitting the power spectrum to an appropriate model. However, fitting the anharmonic overtones is challenging because it is impossible to differentiate between an overtone and a different mode at the same frequency as the overtone. To simplify our formulation, we only consider coupling between different modes and ignore contributions from anharmonic overtones. If we model the classical dynamics as a set of decaying harmonic oscillators (eq 18), then we can compute a set of decay constants (k_j) that correspond to frequencies (ω_j).

$$\langle v_i^2 \rangle = \sum_j V_{ij}^2 e^{i\omega_j t - k_j t} \tag{18}$$

In the observed INS spectrum, anharmonicities cause a decrease in the energetic difference between overtones, meaning that overtones can no longer be calculated via simple Fourier convolution. The goal is to relate the relaxation rates (k_j) to the second order energy correction ($E_j^{(2)}$) found by perturbation theory to correct the overtones. In SI section 2, we derive a natural relationship between the relaxation rate k_i and the second order correction to the harmonic energy levels, $E_i^{(2)}$:

$$\langle k_i \rangle = -\sum_f \frac{4\langle i|V|f\rangle\langle f|V|i\rangle}{\pi\hbar\,(E_f - E_i)} = \frac{4E_i^{(2)}}{\pi\hbar} \tag{19}$$

Given this connection, we can develop a scheme to correct the convolutions to give the proper energetic spacing for an anharmonic oscillator truncated to third order. Importantly, the decay rates determined from a classical simulation correspond to the thermalized initial state, not the vibrational ground state as is typically assumed for computing INS spectra. Correcting for this effect would require multiple classical simulations at different temperatures. While such an implementation is possible, we do not find it practical for large systems of atoms with complex INS spectra, as the harmonic approximation appears to be sufficient.

3 Results

To demonstrate our new approach, we chose to study a semiconducting polymer called P3HT, because it has a complex microstructure owing to its semicrystalline nature. This makes it challenging to experimentally characterize the microstructure and model the functional properties [5, 25]. We used the method presented above to compute an INS spectrum from an MD trajectory and compare to a previously published experimental INS spectrum for semicrystalline P3HT [6]. Since P3HT is known to have amorphous and crystalline regions [25], we perform independent simulations on both phases, and compare to combinations of regioregular (semicrystalline) and regiorandom (fully amorphous) INS spectra. RRa P3HT is a

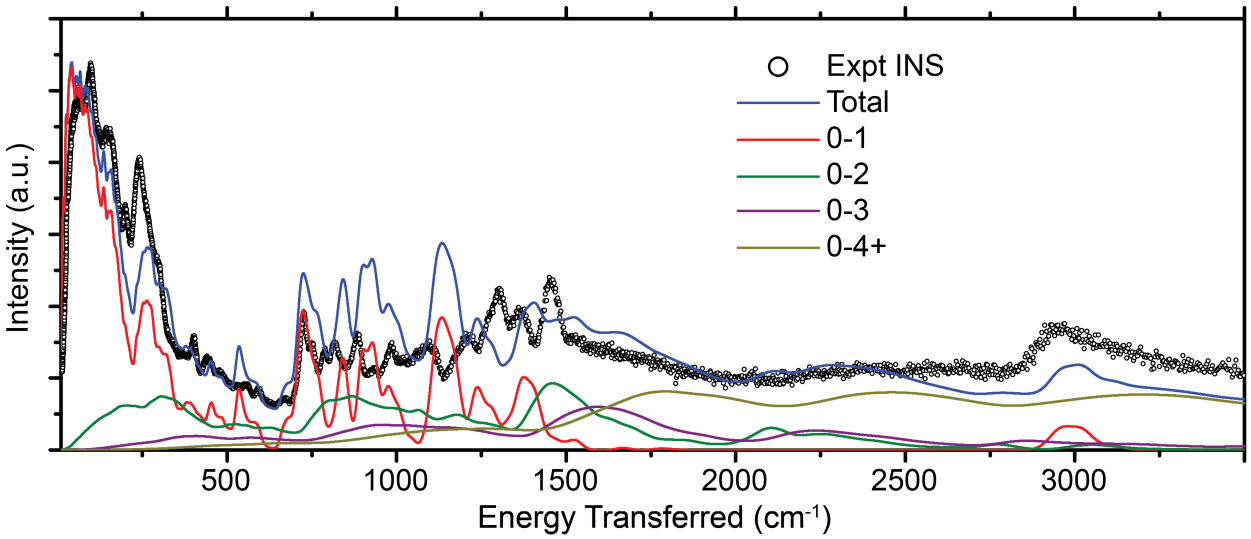

Figure 2: Comparison between experimental INS spectrum for crystalline P3HT (defined as the difference between the semicrystalline spectrum and 55% of the amorphous spectrum) and a simulated spectrum from molecular dynamics. The spectral contributions for individual overtones are also shown. The MD spectrum was convoluted by a Gaussian of width 0.01E, where E is the energy transfer.

surrogate for the amorphous regions of regioregular (RR) P3HT because the random head/tail orientation of the monomers increases dihedral distortions through steric interactions between neighboring sidechains. The increased dihedral distortions reduce the favoring of $\pi - \pi$ stacking/crystalline morphologies.

To simulate the crystalline phase of P3HT, we constructed a box of 16 20-mers created from a larger crystalline structure taken from ref [26] containing 400 chains that was annealed at 300 K and 1 bar for 15 ns. The classical force-field used was taken from Poelking et al. [5], in which the monomer-monomer torsional parameters and partial charges were parametrized from DFT simulations, and standard OPLS-AA forcefield parameters were used for all other values. The lattice parameters for the room temperature crystalline structure agree with prior experimental work [27]. The structure was quenched down to 10 K, and equilibrated for 10 ns, enough time to allow the kinetic temperature to reach 10 K. We were not interested in finding the thermodynamically equilibrated 10 K structure, as the real sample used in the INS experiment was quickly cooled to cryogenic temperatures with liquid helium, kinetically trapping the configurations during the cooling process. After the short equilibration run at low temperature, a production run was started in which we collected velocity data every 2 fs for 100 picoseconds. Such a high data collection rate is needed to resolve higher energy peaks (C-H stretch period is $\sim$ 10 fs). If smaller data collection rates are used, the higher energy peaks will not be resolvable as their frequencies are greater than half of the data collection rate. These high energy peaks are not filtered out of the spectrum, and instead fold back onto the observed spectrum at a different energy, creating unphysical spectral artifacts that contaminate the computed INS spectrum. The choice of 100 ps simulation time leads to a frequency spacing of 0.33 cm^{-1}, which is small enough to resolve any salient features in the experimental INS spectrum. One is free to simulate longer, but the high data collection rate means that the file sizes can become extremely large for systems with many atoms. Further details for all MD simulations are in the Methods section.

The resulting simulated spectrum is compared against the experimental INS spectrum in Figure 2. In addition to the total spectrum, we show the different contributions from each of the overtones. Without any overtones, the simulated spectrum would be equal to the 0-1 spectrum, leading to inaccuracies when comparing to the experimental data. Properly accounting for the overtones allows for quantitative comparisons between theory and experiment, which has applications in direct forcefield parameter fitting.

To demonstrate an improvement over the existing methodology for simulating INS spectra, we compare the MD simulated spectrum against INS data, and a full Brillouin zone DFT calculation of a single conformation of crystalline P3HT in Figure 2. The INS

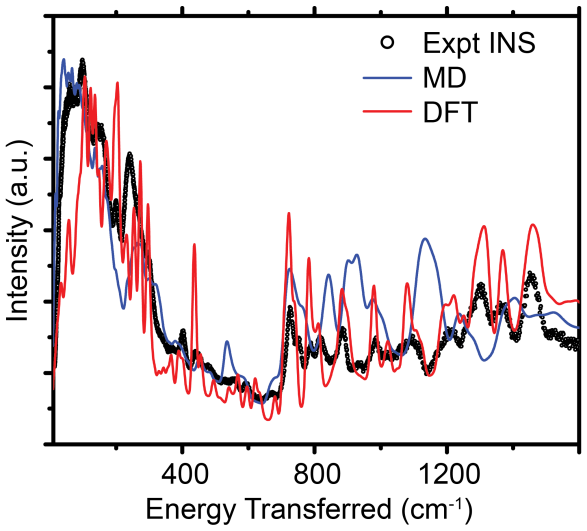

Figure 3: Comparison between experimental INS spectrum, DFT simulated spectrum, and MD simulated spectrum. The MD spectrum was convoluted by a Gaussian of width 0.01E, where E is the energy transfer.

data in Figure 2 is the result of subtracting 55% of a regiorandom P3HT INS spectrum (assumed to be completely amorphous) from the regioregular P3HT spectrum, meaning we are assuming that the P3HT sample is 45% crystalline, which agrees with prior literature [25]. At energies below 600 cm^{-1}, the MD simulation more accurately models the INS spectrum than the DFT simulation. Since prior literature has shown that DFT can accurately simulate INS spectra [15], we can assume that the DFT spectrum is accurate for the chosen configuration, so the MD simulation is more accurate than the DFT simulation because it properly samples the relevant phase space of crystalline P3HT. In the intermediate energy range of 600–1600 cm^{-1}, the MD simulation shows poorer agreement with the experimental INS spectrum than the DFT simulation, indicating that DFT is better at accurately modeling the angle bends/wags, and bond stretch modes present in this energy range. Beyond 1600 cm^{-1}, the experimental spectrum levels off, and there is decent agreement between the simulation and experiment in which the C-H stretch peak at ∼3000 cm^{-1} is well parametrized in the forcefield, and the computed background scattering levels are accurate. The comparison between experiment and both simulations is available in the Supplemental Information Figure S5.

For the amorphous region of P3HT, we started from a box of 800 amorphous 20-mer chains annealed at 300 K, which was taken from Scherer et al. [26]. The average density of the initial structure was 1.05 g/cm^3, which reasonably agrees with prior literature values for the room temperature density of amorphous P3HT [28]. The details for the melting and annealing of the simulation box are in the Methods section. From 300 K, the amorphous system was ramped down to 10 K over 1 μs, and held there for 10 ns. Then, the simulated INS spectrum was computed from a short production run (same as the crystalline simulation), and compared against the crystalline simulated spectrum in Figure 4a. There are significant deviations between the two spectra at low energies, and the change between the two spectra is not consistent with the experimental INS spectrum of regiorandom (RRa) P3HT in Figure 4b. In Figure S4 of the Supplemental Information, we demonstrate that there is very little change at low energies between the experimental INS spectra for RRa P3HT and RR P3HT, indicating a subtle inaccuracy in the MD simulation.

We use a least-squares error statistic weighted by the experimental error of each data point to determine the quality of the agreement between the simulations and the experimental data. The equation for determining the error is given below,

$$E = \frac{1}{N}\sum_{i}^{N}\frac{(x_i - x_i^o)^2}{\sigma_i^2} \tag{20}$$

where x_i and x_i^o are the simulated intensities and experimental intensities at frequency i, respectively, and σ_i is the experimental error at that frequency.

Table 1: Weighted least squares error for the comparisons of the three simulations to the experimental data. E_{low} and E_{high} are the weighted least squares errors for the energy ranges 10 cm^{-1}-600 cm^{-1} and 600 cm^{-1}-3500 cm^{-1}, respectively.

Simulation	E_{low}	E_{high}
Crystalline MD	30.4	23.7
Amorphous MD	53.4	28.5
Crystalline DFT	41.0	17.7

Table 1 compares the weighted least square error for each of the simulations. In the low energy region (10 cm^{-1}-600 cm^{-1}), the crystalline MD simulation more accurately represents the data than the other simulations. This quantitatively demonstrates that the presence of multiple morphologies in the larger MD simulation leads to a more accurate agreement with experimental data for low energy dynamics. In the high energy region (600 cm^{-1}-3500 cm^{-1}),

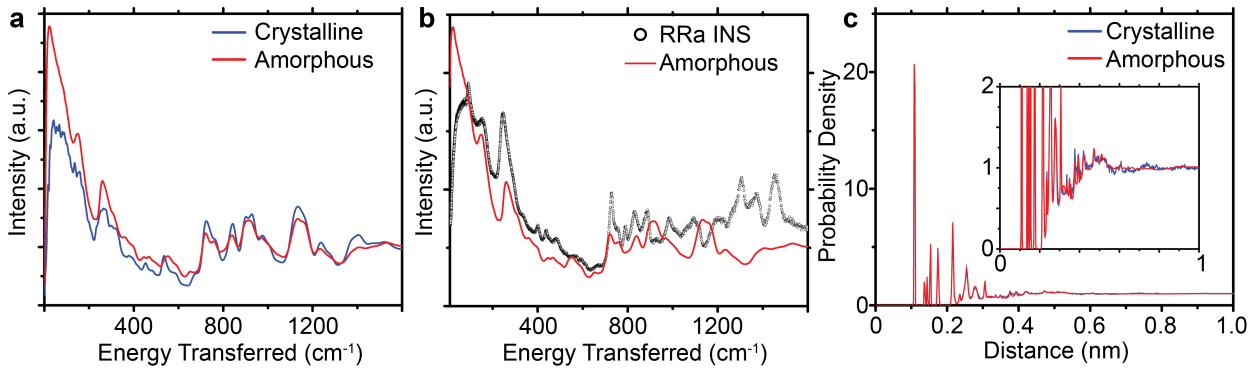

Figure 4: Comparison between MD simulated spectra for crystalline and amorphous P3HT materials. (b) Comparison between experimental INS spectrum for regiorandom (RRa) P3HT, and the amorphous MD simulated spectrum. (c) Radial distribution functions comparing crystalline and amorphous regions of P3HT; the inset is the same plot expanded at low probability densities to demonstrate the differences between the two distributions. The MD spectrum was convoluted by a Gaussian of width 0.01E, where E is the energy transfer.

the crystalline DFT simulation is the most accurate, which makes sense because the classical forcefield has not been modified specifically for the bond vibrations present in P3HT. When comparing the two MD simulations, we see that the amorphous simulation is significantly less accurate than the crystalline one.

There are two possible causes for the changes we observe in the simulated INS spectra: (1) the simulated morphology leads to a lower density than what is observed in reality, and (2) the force field parameters, obtained at room temperature, are not transferable to low temperatures. The answer is likely some combination of both causes. Since low temperature structural studies that measure density are unavailable for P3HT, it is difficult to quantitatively determine the quality of our simulated amorphous morphology. It is possible that the 300 K melt of P3HT chains was not in the correct morphology before the quench; the simulated density was lower than the experimental density (1.05 g/cm^{-1} versus 1.09 g/cm^{-1}). This morphological error led to a lower density for the low temperature morphology, which may partially explain the deviation we see in Figure 4. Any evidence of errors in morphology is largely absent from structural descriptors, like the radial distribution functions in Figure 4c, which demonstrates the sensitivity of low frequency dynamics to subtle changes in morphology.

Also, despite the lack of experimental evidence, we expect that the measured amorphous density is lower than the measured crystalline density at low temperature (the amorphous density is lower than the crystalline density at 300 K [28]), which means that we should see a shift in the low frequency portion of the INS spectra when we compare regioregular and regiorandom P3HT. However, in Figure S4 of the Supplemental Information, there are no observed shifts in the low frequency spectra, indicating that the low frequency dynamics should be relatively invariant to small changes in density. This difference between experimental and simulated trends is likely due to subtle inaccuracies in the non-bonded potential in the force field, which is explained by the lack of transferability of the force field, which was parametrized for 300 K properties, to 10 K simulations.

While there are differences between the low frequency modes in the crystalline and amorphous simulations, both the crystalline/amorphous comparisons with experimental spectra (Figure 3 and Figure 4b, respectively) show that the low energy peaks in the simulated spectra (< 200 cm^{-1}) are lower in energy than the experimental spectra. This provides evidence that there are subtle inaccuracies in the force field parameters at low temperatures that are independent of the simulated morphology. Further neutron experiments (e.g. 300 K INS) and temperature dependent structural studies (e.g. grazing incidence x-ray diffraction) are required to understand if the forcefield accurately characterizes the low energy dynamics at 300 K, which are outside the scope of this work. In principle, the forcefield and morphology inaccuracies can be quantified by using our method in combination with these additional experiments.

4 Conclusions

We have demonstrated a novel method for computing INS spectra from classical molecular dynamics trajectories that is theoretically equivalent to more common normal mode approaches, while being more computationally scalable, allowing simulations of much larger systems than those studied in prior INS publications. As a result, this method opens the door to many research areas that can use INS as an analytical tool, but have not yet done so because the target molecules/materials are too complex for ab initio methods. Our complex example material is semicrystalline P3HT, and we were able to use our method, along with experimental INS data, to make a valuable, direct comparison between experimental and simulated low energy dynamics. Such a direct comparison with molecular dynamics simulations is not possible with other experimental techniques.

In our example, we demonstrated that the simulation of larger scale morphologies of P3HT using molecular dynamics yielded better agreement with experimental INS spectra than crystalline density functional theory simulations in the $10 - 600$ cm^{-1} energy range. In the range beyond 600 cm^{-1}, the DFT simulation is most accurate. Our analysis also revealed potential inaccuracies within some combination of the simulated morphology and the non-bonded parameters of the empirical forcefield of P3HT. We showed that changes in the amorphous density relative to the crystalline density caused large changes in the low frequency dynamics, demonstrating that the low energy region of simulated spectra is sensitive to morphological changes. Therefore, our method provides important information that describes the impact of the forcefield and the simulated non-equilibrium morphologies on low frequency dynamics, which is not accessible by any other combination of simulation and experiment.

Implementation of our method to multiple diverse amorphous and semicrystalline systems provides a basis for more accurate characterization of materials that spans a large area of chemical space. This offers the potential to improve the theoretical understanding of how chemical structure impacts empirical forcefield parameters, which aids the general prediction of observed properties from chemical structure.

5 Methods

Molecular dynamics simulations were performed using the Gromacs simulation package [29, 30, 31] installed on a high-performance computing cluster at UC Davis. Crystalline P3HT simulations began as a slice from a larger crystalline slab generated by Scherer et al. [26], which were equilibrated at 300 K for 15 ns. We then lowered the control temperature of the thermostat to 10 K, and simulated in an NPT ensemble for 10 ns, allowing the kinetic temperature to reach equilibrium. We used a velocity-rescale thermostat [32] with a time constant of 1 ps, and an anisotropic Parrinello-Rahman barostat [33] with damping constants of 1 ps and $4.5 \cdot 10^{-5}$ bar^{-1} in all directions. For the production run in which we simulated the INS spectrum, the thermostat time constant was increased to 10 ps, we switched to an Andersen massive thermostat, we turned off the barostat, and fixed the lattice dimensions to their average values over the final 1 ns of the equilibration run. The 100 ps production runs recorded atomic velocities every 2 fs to properly record every vibrational mode in the material. We switched to the Andersen massive thermostat [34] to properly decorrelate the atomic motions after 10 picoseconds, which ensured the success of our method. However, we ultimately found no dependence on the observed spectrum and the type of thermostat used; see SI section 3. If the time constant is decreased to 1 picosecond, then the thermostat interferes with the simulated INS spectrum, also shown in section 3. The NPT ensemble was not used for production runs because the barostat dampens the dynamics of the molecules (see SI section 3).

The amorphous structure for P3HT was also started from configurations generated by Scherer et al. [26]. We repeat some details here for clarity. For the amorphous region of P3HT, a box of 800 20-mer chains in the crystalline configuration above was simulated at 750 K for $\sim$3.7 ns to randomize all configurations. The box was brought to 300 K by stepping down the temperature by 50 K increments and simulating for 200 ps. Once 300 K was reached, the box was annealed for $\sim$ 61 ns. The average density of the final structure at 300 K was 1.05 g/cm^3, which reasonably agrees with prior literature values [28]. From 300 K, the amorphous system was ramped down to 10 K over 1 μs at a constant rate, and held there for 10 ns. We used an Andersen-massive thermostat with a time constant of 1 ps, and an anisotropic Parrinello-Rahman barostat with the same damping constants as the crystalline quench to 10 K. Then, we averaged the lattice parameters over the latter half of the 10 K NPT hold simulation to fix the lattice parameters for the 100 ps NVE production run, which we used to simulate the INS spectrum.

INS spectra were computed using a Python code developed by our group utilizing mpi4py [35, 36, 37] to parallelize the calculation. All convolution and

correlation operations were performed via Fourier transforms within the Scipy package. The resolution function of the VISION instrument was assumed to be Gaussian with a width that scales with energy transfer as $\sigma = 0.01\Delta E$, where ΔE is the energy transfer. We assumed that the energy of the scattered neutron that hits the detector is fixed at 32 cm^{-1}, which is typical of inverted neutron spectrometers like VISION [17].

6 Acknowledgments

This research was supported by the Department of Energy – Basic Energy Sciences, Award DE-SC0010419, including salary for TFH, MD and AJM. We acknowledge financial support by the DFG through the collaborative research center TRR 146. This research used resources of the National Energy Research Scientific Computing Center, a DOE Office of Science User Facility supported by the Office of Science of the U.S. Department of Energy under Contract No. DE-AC02-05CH11231. The INS spectra were measured at the Spallation Neutron Source, a DOE Office of Science User Facility operated by the Oak Ridge National Laboratory.

References

[1] G. Crabtree, S. Glotzer, B. McCurdy, and J. Roberto, "Computational Materials Science and Chemistry: Accelerating Discovery and Innovation through Simulation-Based Engineering and Science," *Report of the US Department of Energy Workshop on Computational Materials Science and Chemistry for Innovation*, 2010.

[2] A. B. Kayitmazer, D. Seeman, B. B. Minsky, P. L. Dubin, and Y. Xu, "Protein-polyelectrolyte interactions," *Soft Matter*, vol. 9, no. 9, pp. 2553–2583, 2013.

[3] M.-C. Bellissent-Funel, A. Hassanali, M. Havenith, R. Henchman, P. Pohl, F. Sterpone, D. van der Spoel, Y. Xu, and A. E. Garcia, "Water Determines the Structure and Dynamics of Proteins," *Chem. Rev.*, vol. 116, no. 13, pp. 7673–7697, 2016.

[4] C. Bousige, C. M. Ghimbeu, C. Vix-Guterl, A. E. Pomerantz, A. Suleimenova, G. Vaughan, G. Garbarino, M. Feygenson, C. Wildgruber, F.-J. Ulm, R. J. M. Pellenq, and B. Coasne, "Realistic molecular model of kerogen's nanostructure," *Nat Mater*, vol. 15, no. 5, pp. 576–582, 2016.

[5] C. Poelking and D. Andrienko, "Effect of Polymorphism, Regioregularity and Paracrystallinity on Charge Transport in Poly(3-hexylthiophene) [P3HT] Nanofibers," *Macromolecules*, vol. 46, no. 22, pp. 8941–8956, 2013.

[6] T. F. Harrelson, Y. Q. Cheng, J. Li, I. E. Jacobs, A. J. Ramirez-Cuesta, R. Faller, and A. J. Moulé, "Identifying Atomic Scale Structure in Undoped/Doped Semicrystalline P3HT Using Inelastic Neutron Scattering," *Macromolecules*, vol. 50, no. 6, pp. 2424–2435, 2017.

[7] J. B. Klauda, R. M. Venable, J. A. Freites, J. W. O'Connor, D. J. Tobias, C. Mondragon-Ramirez, I. Vorobyov, A. D. MacKerell, and R. W. Pastor, "Update of the CHARMM All-Atom Additive Force Field for Lipids: Validation on Six Lipid Types," *J. Phys. Chem. B*, vol. 114, no. 23, pp. 7830–7843, 2010.

[8] A. A. Latimer, A. R. Kulkarni, H. Aljama, J. H. Montoya, J. S. Yoo, C. Tsai, F. Abild-Pedersen, F. Studt, and J. K. Nørskov, "Understanding trends in C-H bond activation in heterogeneous catalysis," *Nature Materials*, vol. 16, p. 225, 2016.

[9] C. Cuadrado-Collados, J. Fernandez-Catala, F. Fauth, Y. Q. Cheng, L. L. Daemen, A. J. Ramirez-Cuesta, and J. Silvestre-Albero, "Understanding the breathing phenomena in nano-ZIF-7 upon gas adsorption," *J. Mater. Chem. A*, vol. 5, no. 39, pp. 20938–20946, 2017.

[10] X. Han, H. G. W. Godfrey, L. Briggs, A. J. Davies, Y. Cheng, L. L. Daemen, A. M. Sheveleva, F. Tuna, E. J. L. McInnes, J. Sun, C. Drathen, M. W. George, A. J. Ramirez-Cuesta, K. M. Thomas, S. Yang, and M. Schröder, "Reversible adsorption of nitrogen dioxide within a robust porous metal-organic framework," *Nature Materials*, 2018.

[11] S. W. I. Siu, K. Pluhackova, and R. A. Böckmann, "Optimization of the OPLS-AA Force Field for Long Hydrocarbons," *J. Chem. Theory Comput.*, vol. 8, no. 4, pp. 1459–1470, 2012.

[12] S. F. Parker, A. J. Ramirez-Cuesta, and L. Daemen, "Vibrational spectroscopy with neutrons: Recent developments," *Spectrochimica Acta Part A: Molecular and Biomolecular Spectroscopy*, vol. 190, pp. 518–523, 2018.

[13] T. F. Harrelson, A. J. Moulé, and R. Faller, "Modeling organic electronic materials: bridging length and time scales," *Molecular Simulation*, vol. 43, no. 10-11, pp. 730–742, 2017.

[14] N.-E. Lee, J.-J. Zhou, L. A. Agapito, and M. Bernardi, "Charge transport in organic molecular semiconductors from first principles: The bandlike hole mobility in a naphthalene crystal," *Phys. Rev. B*, vol. 97, no. 11, p. 115203, 2018.

[15] T. F. Harrelson, V. Dantanarayana, X. Xie, C. Koshnick, D. Nai, R. Fair, S. A. Nuñez, A. K. Thomas, T. L. Murrey, M. A. Hickner, J. K. Grey, J. E. Anthony, E. D. Gomez, A. Troisi, R. Faller, and A. J. Moulé, "Direct probe of the nuclear modes limiting charge mobility in molecular semiconductors," *Mater. Horiz.*, vol. 6, no. 1, pp. 182–191, 2019.

[16] L. Cai, Y. Shi, K. Hrdina, L. Moore, J. Wu, L. L. Daemen, and Y. Cheng, "Low-temperature vibrational dynamics of fused silica and binary silicate glasses," *Phys. Rev. B*, vol. 97, no. 5, p. 54311, 2018.

[17] P. C. H. Mitchell, S. F. Parker, A. J. Ramirez-Cuesta, and J. Tomkinson, *Vibrational Spectroscopy with Neutrons*, vol. 3 of *Neutron Techniques and Applications*. World Scientific, 2005.

[18] A. J. Ramirez-Cuesta, "aCLIMAX 4.0.1, The new version of the software for analyzing and interpreting INS spectra," *Computer Physics Communications*, vol. 157, no. 3, pp. 226–238, 2004.

[19] Y. Q. Cheng, L. L. Daemen, A. I. Kolesnikov, and A. J. Ramirez-Cuesta, "Simulation of Inelastic Neutron Scattering Spectra Using OCLIMAX," *Journal of Chemical Theory and Computation*, vol. 15, pp. 1974–1982, mar 2019.

[20] O. R. N. Laboratory, "Vibrational Spectrometer - VISION." \url{https://neutrons.ornl.gov/vision}.

[21] L. T. Kong, "Phonon dispersion measured directly from molecular dynamics simulations," *Computer Physics Communications*, vol. 182, no. 10, pp. 2201–2207, 2011.

[22] E. N. Koukaras, G. Kalosakas, C. Galiotis, and K. Papagelis, "Phonon properties of graphene derived from molecular dynamics simulations," *Scientific Reports*, vol. 5, no. 1, p. 12923, 2015.

[23] G. E. Granroth, A. I. Kolesnikov, T. E. Sherline, J. P. Clancy, K. A. Ross, J. P. C. Ruff, B. D. Gaulin, and S. E. Nagler, "SEQUOIA: A Newly Operating Chopper Spectrometer at the SNS," *Journal of Physics: Conference Series*, vol. 251, p. 12058, 2010.

[24] N. W. Ashcroft and N. D. Mermin, *Solid State Physics*. Harcourt College Publishers, 1976.

[25] R. Noriega, J. Rivnay, K. Vandewal, F. P. V. Koch, N. Stingelin, P. Smith, M. F. Toney, and A. Salleo, "A general relationship between disorder, aggregation and charge transport in conjugated polymers," *Nat Mater*, vol. 12, no. 11, pp. 1038–1044, 2013.

[26] C. Scherer and D. Andrienko, "Comparison of systematic coarse-graining strategies for soluble conjugated polymers," *The European Physical Journal Special Topics*, vol. 225, pp. 1441–1461, oct 2016.

[27] N. Kayunkid, S. Uttiya, and M. Brinkmann, "Structural Model of Regioregular Poly(3-hexylthiophene) Obtained by Electron Diffraction Analysis," *Macromolecules*, vol. 43, no. 11, pp. 4961–4967, 2010.

[28] C. S. Lee and M. D. Dadmun, "Important thermodynamic characteristics of poly(3-hexyl thiophene)," *Polymer*, vol. 55, no. 1, pp. 4–7, 2014.

[29] S. Pronk, S. Páll, R. Schulz, P. Larsson, P. Bjelkmar, R. Apostolov, M. R. Shirts, J. C. Smith, P. M. Kasson, D. van der Spoel, B. Hess, and E. Lindahl, "GROMACS 4.5: a high-throughput and highly parallel open source molecular simulation toolkit," *Bioinformatics*, vol. 29, no. 7, pp. 845–854, 2013.

[30] S. Páll, M. J. Abraham, C. Kutzner, B. Hess, and E. Lindahl, "Tackling Exascale Software Challenges in Molecular Dynamics Simulations with GROMACS," in *Solving Software Challenges for Exascale* (S. Markidis and E. Laure, eds.), (Cham), pp. 3–27, Springer International Publishing, 2015.

[31] M. J. Abraham, T. Murtola, R. Schulz, S. Páll, J. C. Smith, B. Hess, and E. Lindahl, "GROMACS: High performance molecular simulations through multi-level parallelism from laptops to supercomputers," *SoftwareX*, vol. 1-2, pp. 19–25, sep 2015.

[32] G. Bussi, D. Donadio, and M. Parrinello, "Canonical sampling through velocity rescaling," *J. Chem. Phys.*, vol. 126, no. 1, p. 14101, 2007.

[33] M. Parrinello and A. Rahman, "Polymorphic transitions in single crystals: A new molecular dynamics method," *Journal of Applied Physics*, vol. 52, pp. 7182–7190, feb 1981.

[34] H. C. Andersen, "Molecular dynamics simulations at constant pressure and/or temperature," *J. Chem. Phys.*, vol. 72, pp. 2384–2393, feb 1980.

[35] L. Dalcín, R. Paz, and M. Storti, "MPI for Python," *Journal of Parallel and Distributed Computing*, vol. 65, no. 9, pp. 1108–1115, 2005.

[36] L. Dalcín, R. Paz, M. Storti, and J. D'Elía, "MPI for Python: Performance improvements and MPI-2 extensions," *Journal of Parallel and Distributed Computing*, vol. 68, no. 5, pp. 655–662, 2008.

[37] L. D. Dalcin, R. R. Paz, P. A. Kler, and A. Cosimo, "Parallel distributed computing using Python," *Advances in Water Resources*, vol. 34, no. 9, pp. 1124–1139, 2011.